Topological effects on transition temperatures and response functions in three-dimensional Fermi superfluids

Brandon M. Anderson, Chien-Te Wu, Rufus Boyack, and K. Levin

Phys. Rev. B **92**, 134523 — Published 26 October 2015

DOI: 10.1103/PhysRevB.92.134523

Topological effects on transition temperatures and response functions in three-dimensional Fermi superfluids

Brandon M. Anderson,* Chien-Te Wu, Rufus Boyack, and K. Levin

James Franck Institute, University of Chicago, Chicago, Illinois 60637, USA

We investigate the effects of topological order on the transition temperature, T_c, and response functions in spin-orbit coupled fermionic superfluids with a transverse Zeeman field in three dimensions. Our calculations include fluctuation effects beyond mean-field theory and are compatible with f-sum rules. In the topological phase we find that T_c can be as large as 10% of the Fermi temperature, which should be experimentally accessible in cold gas experiments. At higher temperatures, above T_c, the spin and density response functions provide signatures of topological phases via the recombination or amplification of frequency dependent peaks.

The excitement surrounding topological superfluids[1–4] derives from both their scientific as well as technological potential. Inspired by the canonical topological superfluid, a spinless p_x+ip_y superfluid[1], it has been argued[5–7] that some combination of spin-orbit coupling (SOC), Zeeman field, as well as superfluid pairing can artificially produce such a state. This was explored via the proximity effect[5] in solid state systems and using intrinsic pairing in ultracold atomic Fermi gases[6,8–11].

In the present paper we address this second case of intrinsic pairing. A central goal is to determine how a transition from a trivial to a topological phase is reflected in the superfluid transition temperature T_c. This is particularly important since cold gas experiments have now implemented spin-orbit coupling[12–14] and, if T_c is sufficiently large, will be able to address topological phases. Calculations of T_c in a topological phase which, necessarily go beyond previous[15–21] mean-field approaches, are not available. Indeed, topological order at the transition is only a meaningful concept if T_c, itself, is computed in the presence of a pairing gap. Thus, here we emphasize the importance of fluctuations. In a topological phase we find that T_c can be as large as 10% of the Fermi temperature (T_F) which should be quite accessible experimentally. However, we find that these superfluids self-consistently adjust to stabilize topological phases in the lower T_c, BCS regime.

In addition to T_c, it is important to establish signatures of topological order as reflected in the band-structure. While there have been a number of proposals in the literature[16,17,22–25] we approach this challenge via studies of the finite temperature density-density and spin-spin correlation functions, which should be accessible[26] in future experiments. We find that the position or threshold of peaks in these responses reflects the topological nature of the band-structure. Importantly, these response functions are tightly constrained by sum rules. Our theoretical framework satisfies all sum rules, which serves as a check on our calculations and implies these signatures of topological order in response functions are unambiguous. In the topological phase we find that a peak in the density response is significantly amplified due to a saddle point Van Hove singularity, often seen in correlated superfluids[27,28]. In the trivial phase the spin response exhibits two distinct peaks, which merge into a single peak in the topological phase.

Topological superfluids.– The concept of topological order is based on the Bogoliubov or fermionic quasiparticle dispersion associated with a mean-field approximation. We therefore begin with the Bogoliubov-de Gennes (BdG) Hamiltonian for a spin-orbit coupled superfluid:

$$\mathcal{H}_{\mathrm{BdG}} = \begin{pmatrix} H_0(\mathbf{k}) & \Delta \\ \Delta^* & -\widetilde{H}_0(\mathbf{k}) \end{pmatrix}, \tag{1}$$

where Δ is a pairing gap and $\widetilde{H}_0(\mathbf{k}) = \sigma_y [H_0^*(-\mathbf{k})] \sigma_y$ is the time-reversed single-particle (hole) Hamiltonian. Here the single particle Hamiltonian $H_0(\mathbf{k}) = \xi_{\mathbf{k}} + \mathbf{h}(\mathbf{k}) \cdot \boldsymbol{\sigma}$, where $\xi_{\mathbf{k}} = k^2/2m - \mu$ describes a free particle of momentum $\mathbf{k} = (k_x, k_y, k_z)$, mass m, and chemical potential μ; throughout we set $\hbar = k_B = 1$. The spin-orbit coupling enters through the vector $\mathbf{h}(\mathbf{k}) = \mathbf{h}_\perp(\mathbf{k}) + \mathbf{h}_\parallel(\mathbf{k})$ that couples the spin-1/2 operator $\boldsymbol{\sigma} = (\sigma_x, \sigma_y, \sigma_z)$ to a Zeeman field $\mathbf{h}_\parallel(\mathbf{k}) = b_z \hat{z}$ and an in-plane SOC field $\mathbf{h}_\perp(\mathbf{k}) = \lambda \mathbf{k}_\perp / m$, with SOC strength λ.

Of significant theoretical interest has been isotropic (Rashba) SOC, described by $\mathbf{k}_\perp = (k_x, k_y, 0)$ with an out-of-plane momentum $\mathbf{k}_\parallel = \mathbf{k} - \mathbf{k}_\perp = (0, 0, k_z)$; in the main text we primarily consider this Rashba case. Note that most experimental success[12,13] has related to the crossed-Raman configuration[29,30] where $\mathbf{k}_\perp = (k_x, 0, 0)$ and $\mathbf{k}_\parallel = (0, k_y, k_z)$. We also considered this case; the mathematical analysis is identical after appropriate redefinition of $\mathbf{k}_\perp$ and $\mathbf{k}_\parallel$, and the results are rather similar.

There are four branches in the BdG eigenvalue spectrum, $\eta E_{\alpha\mathbf{k}}$ for $\alpha, \eta = \pm 1$ with the positive energy dispersion

$$E_{\alpha\mathbf{k}} = \sqrt{\xi_{\mathbf{k}}^2 + |\mathbf{h}|^2 + \Delta^2 + 2\alpha \sqrt{\xi_{\mathbf{k}}^2 |\mathbf{h}|^2 + \Delta^2 b_z^2}}. \tag{2}$$

For the three-dimensional case, this leads to three distinct topological phases. The topological phase diagram is specified by inequalities derived from solving

$E_-(\mathbf{k}_\parallel, \mathbf{k}_\perp = 0) = 0$. No nodes appear when $b_z < \Delta$, corresponding to a non-topological or "trivial" superfluid. If $\mu > 0$ and $(\mu^2 + \Delta^2) > b_z^2 > \Delta^2$, the topological superfluid has four nodes (4-Weyl points) which emerge at $k_\parallel^2 = \mu \pm \sqrt{b_z^2 - \Delta^2}$. Finally, for arbitrary μ, the system is a topological superfluid with two nodes (2-Weyl points) when $b_z^2 > (\mu^2 + \Delta^2)$[15,16,24]. For Rashba SOC, the dispersion around the nodes is linear in momentum, and is described by a Weyl Hamiltonian with topologically protected nodes. For the crossed-Raman scheme the Weyl points are instead topologically protected nodal rings[24].

Along with the usual number equation determining μ, central to a mean-field theory is the self consistent condition or gap equation [15,16,24], which determines Δ. We rewrite this suggestively as

$$\Gamma^{-1}(0,T) = \frac{1}{2}\sum_{\mathbf{k}}\sum_{\eta\alpha\alpha'} \frac{\delta_{\eta,+1} - (\eta f(E_{\alpha\mathbf{k}}) + f(\xi_{\alpha'\mathbf{k}}))}{\eta E_{\alpha\mathbf{k}} + \xi_{\alpha'\mathbf{k}}} \times v_{\eta\alpha\alpha'}(\mathbf{k},\mathbf{k}) + g^{-1} = 0, \quad (3)$$

where $f(x)$ is a Fermi distribution and $g < 0$ is an attractive interaction. Where relevant, we regularize integrals by introducing a scattering length defined through $g^{-1} = m/4\pi a - \sum_{\mathbf{k}} m/\mathbf{k}^2$[31]. The coherence factor $v_{\eta\alpha\alpha'}(\mathbf{k},\mathbf{k})$ (and its generalization, $v_{\eta\alpha\alpha'}(\mathbf{k},\mathbf{k}-\mathbf{q})$), is presented in the Appendix. Their specific form is irrelevant for the present discussion.

Fluctuation Formalism.– The transition temperature, T_c, necessarily contains fluctuation effects[32,33] which serve to distinguish it from the lowest temperature, denoted T^*, at which the mean-field gap equation satisfies $\Delta(T^*) = 0$. The fluctuations in question are non-condensed pairs[32,34]. We choose these pairs in a specific manner[32] to satisfy the Hugenholtz-Pines constraint, making use of Eq. (3). Requiring that these pair excitations are gapless in the ordered phase, we extend Eq. (3) to finite $Q \equiv (i\omega, \mathbf{q})$ (where $i\omega$ is a Bosonic Matsubara frequency) which leads to:

$$\Gamma^{-1}(Q,T) = \frac{1}{2}\sum_{\mathbf{k}}\sum_{\eta\alpha\alpha'} \frac{\delta_{\eta,+1} - (\eta f(E_{\alpha\mathbf{k}}) + f(\xi_{\alpha'\mathbf{k}-\mathbf{q}}))}{(\eta E_{\alpha\mathbf{k}} + \xi_{\alpha'\mathbf{k}-\mathbf{q}}) - i\omega} \times v_{\eta\alpha\alpha'}(\mathbf{k},\mathbf{k}-\mathbf{q}) + g^{-1}. \quad (4)$$

From the structure of Eq. (3) it is apparent that $\Gamma(0,T)$ depends on both the full energy spectrum $E_{\alpha\mathbf{k}}$ as well as the bare energy $\xi_{\alpha\mathbf{k}}$. Thus, one might expect (as implemented in Eq. (4)), that the fluctuation propagator $\Gamma(Q,T)$ should depend on an asymmetric combination of bare and dressed Green's functions[35].

We next consider the propagator in Eq. (4) expanded at small momenta, where (using Eq. (3)) $\Gamma(Q,T) \approx a_0^{-1}(i\omega - \omega_{\mathbf{q}})^{-1}$. Here temperature dependent $a_0 = \left(\partial_{i\omega}\Gamma^{-1}(Q,T)\right|_{Q=0}$ and the T dependent pair dispersion is $\omega_{\mathbf{q}} = a_0^{-1}\left(\Gamma^{-1}(\mathbf{q},T) - \Gamma^{-1}(0,T)\right) \approx q_\perp^2/2M_\perp + q_\parallel^2/2M_\parallel$. We identify $M_\perp$ ($M_\parallel$) as the effective pair mass for the component of momentum parallel (perpendicular) to the SOC vector. While it is sometimes possible to calculate the effective pair masses $M_\perp$, $M_\parallel$ analytically, in general this is not necessary. Rather, it suffices to calculate numerically the second-order derivative at small $\mathbf{q}$[36].

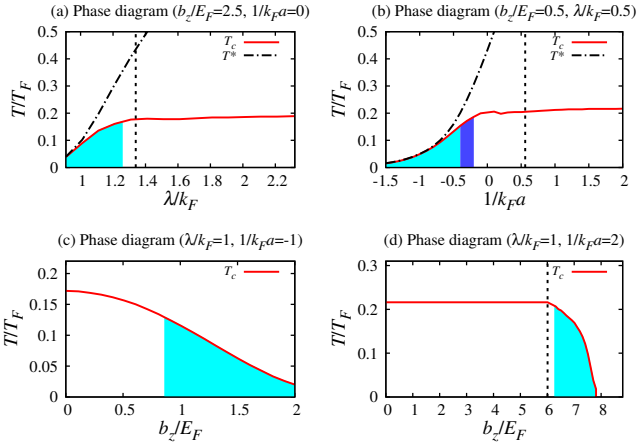

FIG. 1. Phase diagrams for the superfluid temperature T_c and (where shown) the mean-field transition temperature T^*. The $T = 0$ topological phases are indicated by shaded regions in light (dark) blue color with 2 (4)-Weyl points. The top two panels show the dependence on either SOC strength λ (left) or scattering length $1/k_Fa$ (right), with other parameters fixed. The lower panels show T_c versus b_z with $\lambda/k_F = 1$ for both panels, $1/k_Fa = -1$ on the left and $1/k_Fa = 2$ on the right. Dotted lines indicate $\delta\mu = 0$. Once a topological phase is entered the system becomes more BCS-like.

Notice that the small-Q form of $\Gamma(Q,T)$ reflects, up to a constant, the non-interacting Green's function of a thermal Bose gas with pair dispersion $\omega_{\mathbf{q}}$, at or below the condensation temperature ($\Gamma^{-1}(0, T \leq T_c) = 0$). We can relate $\sum_Q \Gamma(Q,T)$ to a quantity proportional to the Bose occupation number n_B and write:

$$-\sum_Q \Gamma(Q,T) = a_0^{-1} n_B = \Delta^2, \quad \text{at } T = T_c. \quad (5)$$

This last equality, which constrains $\Gamma(Q,T_c)$ follows from the fermionic self-energy. It characterizes the excitation gap in the limit in which all pairs are non-condensed. The condition for T_c is then simply obtained[32–34] by equating the constraint on $\Delta(T_c)$ via Eq. (5) with that obtained from the mean-field gap equation in Eq. (3).

Importantly, this approach, which can be generalized to *any* BCS-BEC mean-field theory, explicitly avoids the nonphysical first order transition found in all other BCS-BEC theories[37]. Interpreting Eq. (3) and Eq. (5), we see that Eq. (3) is equivalent to setting the bosonic chemical potential to zero below T_c and Eq. (5) guarantees that the number of non-condensed bosons reaches a maximum at T_c (which is determined by the fermionic pairing gap). We will assume throughout that, above T_c, the mean-field gap represents a reasonable (but not essential) approximation[38] for the normal state Δ.

Phase diagram.– To understand the effects of SOC and the Zeeman field on condensation and pairing, we

numerically compute T^* and T_c, varying $1/k_Fa$, b_z, and λ. Where relevant, we measure quantities in terms of the Fermi momentum (k_F), energy (E_F), or temperature (T_F) as defined with respect to the $\lambda = b_z = 0$ limit. It is convenient to define a shifted chemical potential, $\delta\mu = \mu - \mu_0$, where $\mu_0 = -E_{\rm so}(1 + b_z^2/E_{\rm so}^2)/2$ if $E_{\rm so} \geq b_z$ and $\mu_0 = -b_z$ if $E_{\rm so} < b_z$; here the SOC energy is $E_{\rm so} = \lambda^2/m$. In this way, a necessary (but not sufficient) condition for a topological phase is that $\delta\mu > 0$.

Figure 1 plots T_c and (in some cases) the pairing onset temperature T^* as a function of either λ, b_z or $1/k_Fa$. Dotted lines indicate where $\delta\mu = 0$. Where relevant, these plots are consistent with earlier work[23]. A close analogy between varying λ and varying $1/k_Fa$ is seen in Fig. 1(a) and Fig. 1(b). We define "weak" or "enhanced" pairing relative to $b_z = 0$. The former is associated with small λ or negative $1/k_Fa$ while the latter corresponds to either large λ or large positive $1/k_Fa$. Thus, Fig. 1(c) is characteristic of the generic weak pairing regime while Fig. 1(d) is characteristic of the strong pairing case produced by either large $1/k_Fa$ or large λ.

We analyze the top two figures by focusing on a decreasing abscissa which effects a transition from a trivial to topological phase (shown as shaded). In Fig. 1(a), corresponding to $1/k_Fa = 0$ and $b_z = 2.5E_F$, this transition is driven by varying the SOC strength λ. In Fig. 1(b) it is driven directly by varying the scattering length $1/k_Fa$; somewhat after the point $\delta\mu > 0$ is crossed, a further *decrease* in $1/k_Fa$ (towards the BCS limit) allows the system to reach a topological phase. Here we see a series of two transitions from topologically trivial to 4-Weyl and then to 2-Weyl superfluids. While there is some initial decline in T_c with diminishing $1/k_Fa$, the most significant decrease in T_c occurs in the 2-Weyl case.

The next two panels contrast the regime of weak pairing (Fig. 1(c)) with that of enhanced pairing (Fig. 1(d)). In the first case, the system is BCS-like everywhere. Increasing b_z gradually suppresses T_c and there is no clear signature in T_c of the change from a trivial to a topological phase (shown as shaded in the figure). As shown in Fig. 1(d), when the pairing is enhanced, T_c becomes insensitive to variations in the Zeeman field until $\delta\mu = 0$. Shortly thereafter, the topological phase transition is crossed and T_c rapidly declines.

We can see from the last figure, in particular, that the satisfaction of the topological inequality and the $\delta\mu = 0$ condition importantly define a transition (often quite sharp, as in Fig. 1(d)) between a superfluid, characterized by a larger gap, and larger pair mass, $M_\perp \sim 2m$ (i.e., more "BEC-like"), and a superfluid with a small gap, $\Delta/E_F \ll 1$, and a small pair mass $M_\perp \ll m$ which is "BCS-like". The resulting behavior of T_c arises in the topological phase because there is a competition between the effects of a decreasing pair mass and a decreasing mean-field pairing gap as b_z increases. The net effect is a lowering of T_c in the topological phase. This can, in turn, be viewed as a form of BEC-BCS transition.

One can inquire as to why the topological transition becomes more apparent (as reflected in T_c) on the strong pairing side (Fig. 1(d)), whereas it is less evident (from the perspective of T_c) when in the weak pairing limit (Fig. 1(c)). These differences are reflected in the evolution of the band-structure via a Van Hove singularity as the topological transition is crossed. To address this, Fig. 2 presents a constant energy contour plot for the band $+E_{-1,\mathbf{k}}$. The two axes correspond to the in-plane ($k_\perp$) and out-of-plane ($k_\parallel$) momenta. For definiteness, we have chosen $1/k_Fa = 0$ and $\mu(T)$, $\Delta(T)$ are determined for a temperature just above T_c. Local extrema in this figure reflect Van Hove singularities, either at isolated points or extended in a ring-like structure. Each of the three panels in a given row corresponds to increasing values of b_z with only the left-most figures in the trivial phase. The top three figures are in the weak pairing regime whereas the bottom three figures are in the regime of enhanced pairing.

A key observation from these figures is that in the weak pairing limit there is a smooth evolution from a trivial to topological phase, whereas for enhanced pairing the band-structure evolves rather dramatically from a trivial and BEC-like phase to a topological and BCS-like phase. Indeed, the topological transition in the lower panel is roughly correlated with the appearance of additional Van Hove singularities (as indicated). This is in contrast to the upper panel where Van Hove singularities of the trivial and topological phases are relatively unchanged. These figures help interpret the behavior observed in Fig. 1(c) and Fig. 1(d).

Frequency dependent spin and density response functions.– It is important to establish tightly constrained experimental signatures of topological order. There are proposals in the literature which suggest that the topological phase might be observed in atomic Fermi gases through the compressibility κ[16,22,23] or via radio frequency (RF) based probes[17]. However, changes in κ appear to reflect topology only in the limit of small SOC[16,23]. RF experiments in principle measure the electronic dispersion, but resolution and finite temperature broadening effects are not yet[39] well controlled. Our approach is to study density and spin responses, and their associated sum rules.

Here, as in previous work[33] we consider the correlation functions (above T_c) given by

$$\chi_{S_iS_j}(i\omega, \mathbf{q}) = \sum_{\mathbf{k}} \sum_{\alpha\alpha',\eta\eta'} \left(\frac{f(\eta E_{\alpha\mathbf{k}}) - f(\eta' E_{\alpha'\mathbf{k}+\mathbf{q}})}{\eta E_{\alpha\mathbf{k}} - \eta' E_{\alpha'\mathbf{k}+\mathbf{q}} + i\omega} \right) \times w_{\alpha\alpha',\eta\eta'}(\mathbf{k}, \mathbf{k}+\mathbf{q}). \quad (6)$$

The density-density correlation function $\chi_{\rho\rho}(Q)$ corresponds to $i = j = 0$, with $\sigma_0 = \mathbb{1}_2$, whereas $i, j \in \{x, y, z\}$ gives the corresponding spin-spin correlation function. The differences between the density or spin responses are the coherence factors $w_{\alpha\alpha',\eta\eta'}(\mathbf{k}, \mathbf{k}+\mathbf{q})$, which are rather complicated and are presented in the Appendix. As a numerical check on these calculations, the f-sum rule for the density response and related sum rules[33] for

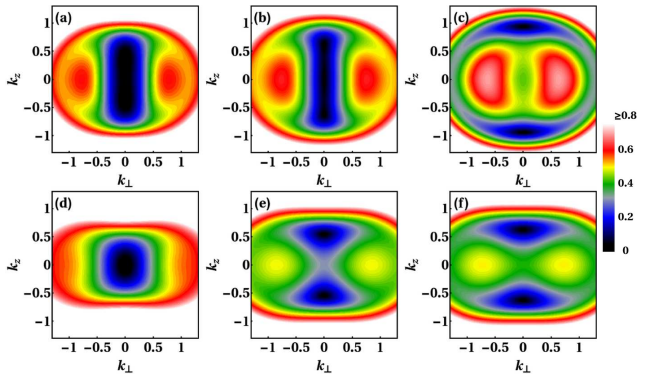

FIG. 2. Evolution of the dispersion as the topological transition is crossed by tuning b_z. In the weak pairing limit (top panel), the system smoothly evolves across the transition, whereas for enhanced pairing (bottom panel) there is a more abrupt change in band-structure. In all plots we show constant energy contours $+E_{-1,\mathbf{k}}/E_F$ at unitarity, with $k_\perp$ and $k_\parallel$ in units of k_F. For panels (a)-(c) we set $\lambda/k_F = 0.5$ and the Zeeman field $b_z/E_F = 0.4, 0.6, 0.8$, whereas for panels (d)-(f) we set $\lambda/k_F = 1$ and $b_z/E_F = 1.2, 1.7, 1.8$ respectively. Only the left-most figures are in a trivial phase.

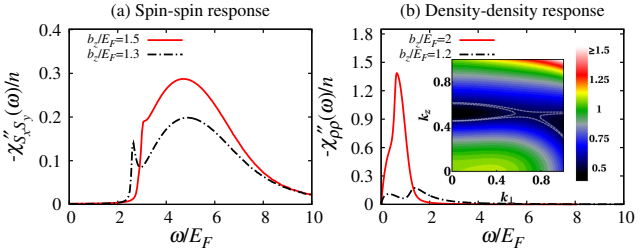

FIG. 3. Contrast between topological (solid, red) and trivial (dashed, black) phases of the frequency dependent spin-spin (Fig. 3(a)) and density-density (Fig. 3(b)) correlation functions. Both response functions are calculated at $1/k_F a = 0$ and $\lambda/k_F = 1$, with respective wave-vectors of $\mathbf{q} = 0$ and $\mathbf{q} = 0.5k_F\hat{z}$ for the spin and charge responses. The inset in Fig. 3(b) shows the energy contours of $E^{(2,+)}(\mathbf{k},\mathbf{q})/E_F$ in the topological phase, with $k_\perp$ and $k_\parallel$ in units of k_F. The dashed lines highlight the saddle point Van Hove singularity whose magnitude determines the frequency location of the peak response in Fig. 3(b).

the spin response hold for all $\mathbf{q}$.

Quite generally, the correlation functions for a paired normal state can be decomposed into two parts; one involving the difference: $E^{(2,-)}(\mathbf{k},\mathbf{q}) = |E_{-1,\mathbf{k}} - E_{\pm 1,\mathbf{k}+\mathbf{q}}|$ which enters as a thermal contribution (at $T \neq 0$), and the other involving the sum: $E^{(2,+)}(\mathbf{k},\mathbf{q}) = |E_{-1,\mathbf{k}} + E_{\pm 1,\mathbf{k}+\mathbf{q}}|$, which we call the multiparticle contribution. We address the $\mathbf{q} = 0$ spin response, $\chi_{S_iS_j}(\omega, 0)$, (where i, j are x or y) so that inter-band terms dominate. Thus, for the ± 1 subscript in the density response, the -1 band label yields the main contribution, whereas in the spin response the $+1$ band label is most important.

Figure 3(a) shows $\chi_{S_xS_y}(\omega, 0)$ for both the trivial and topological phases. In the trivial phase there are two clearly resolvable peaks; the first peak is associated with the thermal contribution and the second with the multiparticle contribution. By contrast, there is only one peak in the topological phase. A related signature for the Hall conductivity (in 2D) at $T = 0$, rather than, as here, above T_c, was suggested earlier[25].

Importantly, this provides a means of distinguishing between the trivial and topological phases. We can analytically identify the position of the maximum in the first (thermal) peak, which is due to a flat band in $E^{(2,-)}(\mathbf{k}, 0)$, and appears at precisely $2b_z$. The threshold for the second peak is $\omega_1 \equiv \min_{\mathbf{k}} E^{(2,+)}(\mathbf{k}, 0)$. In the trivial phase we find that, if $\mu > 0$, $\omega_1 = 2\Delta$, whereas if $\mu < 0$, $\omega_1 = 2(\Delta^2 + \mu^2)^{1/2}$. Hence ω_1 is strictly greater than the frequency of the first peak ($2b_z$), thus yielding two distinct peaks in the response function. In the topological phase, $\omega_1 = 2b_z$ so that the two peaks merge.

We now focus on the density-density correlation function $\chi_{\rho\rho}(\omega, \mathbf{q})$, which is only non-zero when $\mathbf{q} \neq 0$. This is shown in Fig. 3(b) for the case of unitarity: $1/k_F a = 0$, and we can again compare the trivial and topological phases. Here $\lambda/k_F = 1$ and we plot the imaginary part of the response function, $\chi''_{\rho\rho}(\mathbf{q},\omega)$[33], deep in the topological phase ($b_z/E_F = 2$) and in the trivial phase ($b_z/E_F = 1.2$) at $\mathbf{q} = 0.5k_F\hat{z}$ and $T = 0.21T_F$ (just above T_c).

In the trivial phase there are two peaks, one associated with thermal contributions involving $E^{(2,-)}(\mathbf{k},\mathbf{q})$ and the second with the multiparticle component involving $E^{(2,+)}(\mathbf{k},\mathbf{q})$. In the topological phase, there is a large peak at $\omega/E_F = 0.6$, which arises from a (2D) saddle point Van Hove singularity contribution in $E^{(2,+)}(\mathbf{k},\mathbf{q})$. This is associated with $\nabla_{\mathbf{k}} E^{(2,+)}(\mathbf{k},\mathbf{q}) = 0$, which (via the density of states) enters as a denominator in the the response functions. These saddle point Van Hove singularity effects are well known[27,28] and are illustrated in the inset on the right. Importantly, here we observe that as the system enters the topological phase they amplify the peaks in the density-density correlation function, thus helping to distinguish between the trivial and topological phases.

Conclusions.– This paper addresses how an intrinsically produced condensation temperature varies across a topological transition, induced by varying SOC, Zeeman coupling, or the scattering length. Importantly, the introduction of fluctuations necessarily introduces a feedback of the topological band-structure into T_c. The passage from the trivial to the topological phase is accompanied by a transition in which the system is driven towards a low T_c, more BCS-like phase with smaller pair mass and smaller gap. Nevertheless, there is a range of b_z in the topological phase where $T_c \sim 0.1T_F$, which is experimentally accessible[31].

Because of difficulties in cooling in current experiments, we also present methods of detecting the topological band-structure above T_c, exploiting frequency dependent peaks in the density and spin responses. The

topological transition appears in the spin response as a recombination of two peaks, which are separate in the trivial phase. In the topological superfluid, the dynamical density response exhibits a greatly amplified peak associated with a (2D) saddle point Van Hove singularity.

Acknowledgements.– This work was supported by NSF-DMR-MRSEC 1420709.

Note added.– Recently, we became aware of a complementary paper that considers fluctuation effects in spin-orbit coupled superfluids with fixed relative population density using a closely related formalism[40].

I. APPENDIX: DERIVATION OF THE VERTEX FUNCTION $\Gamma(Q)$ AND COHERENCE FACTORS

Here we present derivations of the vertex function $\Gamma(Q)$, where $Q \equiv (i\omega, \mathbf{q})$, along with the coherence factors $v_{\eta\alpha\alpha'}(\mathbf{k}, \mathbf{k}-\mathbf{q})$ and $w_{\alpha\alpha',\eta\eta'}(\mathbf{k}, \mathbf{k}+\mathbf{q})$, which appear in Eq. (4) and Eq. (6) of the main text. We begin by writing the non-interacting Green's function in terms of projectors as follows

$$G_0(K) = \sum_{\alpha} \frac{P^0_{\alpha}(\mathbf{k})}{i\nu - \xi_{\alpha\mathbf{k}}}, \tag{7}$$

where $K \equiv (i\nu, \mathbf{k})$ and $P^0_{\alpha}(\mathbf{k}) = \frac{1}{2} U_{\mathbf{k}} (1 + \alpha\sigma_z) U^{\dagger}_{\mathbf{k}}$ is a projector into the band $\alpha = \pm 1$. The unitary matrix $U_{\mathbf{k}}$ is the unitary operator that diagonalizes $H_0(\mathbf{k})$ to produce the single particle dispersion $\xi_{\alpha\mathbf{k}} = \xi_{\mathbf{k}} + \alpha|\mathbf{h}|$.

Similarly, the Nambu Green's function $\mathcal{G}(K)$ for a superfluid can be written in terms of projectors as

$$\begin{aligned} \mathcal{G}(K) &= [i\nu - H_{\mathrm{BdG}}(\mathbf{k})]^{-1} \\ &= \begin{pmatrix} G(K) & F(K) \\ \widetilde{F}(K) & \widetilde{G}(K) \end{pmatrix} \\ &= \sum_{\alpha\eta} \frac{\mathcal{P}_{\eta\alpha}}{i\nu - \eta E_{\alpha\mathbf{k}}}, \end{aligned} \tag{8}$$

where we have used the inverse of the BdG Hamiltonian, H_{BdG}, to define the normal and anomalous Green's functions $G(K)$ and $F(K)$, along with their time-reversed counterparts $\widetilde{G}(K) = i\sigma_y [G(-K)]^T i\sigma_y$ and $\widetilde{F}(K) = i\sigma_y [F(-K)]^T i\sigma_y$. The projectors $\mathcal{P}_{\eta\alpha} = \psi_{\eta\alpha}\psi^{\dagger}_{\eta\alpha}$ are constructed from the BdG eigenvectors

$$\psi_{\eta\alpha} = \mathcal{U}_{\mathbf{k}} \begin{pmatrix} \alpha\sqrt{\frac{1}{2}\left(1 + \alpha\frac{\xi_{\mathbf{k}}}{E_{0\mathbf{k}}}\right)}\sqrt{\frac{1}{2}\left(1 + \alpha\eta\frac{\zeta_{\alpha\mathbf{k}}}{E_{\alpha\mathbf{k}}}\right)} \\ \eta\sqrt{\frac{1}{2}\left(1 - \alpha\frac{\xi_{\mathbf{k}}}{E_{0\mathbf{k}}}\right)}\sqrt{\frac{1}{2}\left(1 - \alpha\eta\frac{\zeta_{\alpha\mathbf{k}}}{E_{\alpha\mathbf{k}}}\right)} \\ \alpha\eta\sqrt{\frac{1}{2}\left(1 + \alpha\frac{\xi_{\mathbf{k}}}{E_{0\mathbf{k}}}\right)}\sqrt{\frac{1}{2}\left(1 - \alpha\eta\frac{\zeta_{\alpha\mathbf{k}}}{E_{\alpha\mathbf{k}}}\right)} \\ \sqrt{\frac{1}{2}\left(1 - \alpha\frac{\xi_{\mathbf{k}}}{E_{0\mathbf{k}}}\right)}\sqrt{\frac{1}{2}\left(1 + \alpha\eta\frac{\zeta_{\alpha\mathbf{k}}}{E_{\alpha\mathbf{k}}}\right)} \end{pmatrix}, \tag{9}$$

where $\mathcal{U}_{\mathbf{k}} = \mathrm{diag}\{U_{\mathbf{k}}, V_{\mathbf{k}}\}$ rotates the particle (hole) sector to the spin-orbit basis with a unitary matrix $U_{\mathbf{k}}$ ($V_{\mathbf{k}}$), and we have defined $\theta = \cos^{-1}(b_z/|\mathbf{h}|)$, $E_{0\mathbf{k}} = \sqrt{\xi^2_{\mathbf{k}} + \Delta^2\cos^2\theta}$, and $\zeta_{\alpha\mathbf{k}} = E_{0\mathbf{k}} + \alpha|\mathbf{h}|$. Note that $\zeta_{\alpha\mathbf{k}}$ limits to $\xi_{\alpha\mathbf{k}}$ as $\Delta \to 0$ or $b_z \to 0$, and to $\sqrt{\xi^2_{\mathbf{k}} + \Delta^2} + \alpha b_z$ as $\lambda \to 0$.

For convenience, the 4×4 projector matrices can be expressed as four 2×2 sub-matrices as

$$\mathcal{P}_{\eta\alpha}(\mathbf{k}) \equiv \begin{pmatrix} P_{\eta\alpha}(\mathbf{k}) & Q_{\eta\alpha}(\mathbf{k}) \\ R_{\eta\alpha}(\mathbf{k}) & S_{\eta\alpha}(\mathbf{k}) \end{pmatrix}. \tag{10}$$

The Green's function $G(K)$ is found from the appropriate 2×2 sub-matrix with the corresponding projector

$$P_{\eta\alpha}(\mathbf{k}) = \frac{1}{4E_{0\mathbf{k}}E_{\alpha\mathbf{k}}} U_{\mathbf{k}} \begin{pmatrix} (E_{0\mathbf{k}} + \alpha\xi_{\mathbf{k}})(E_{\alpha\mathbf{k}} + \alpha\eta\zeta_{\alpha\mathbf{k}}) & \alpha\Delta^2\sin\theta\cos\theta \\ \alpha\Delta^2\sin\theta\cos\theta & (E_{0\mathbf{k}} - \alpha\xi_{\mathbf{k}})(E_{\alpha\mathbf{k}} - \alpha\eta\zeta_{\alpha\mathbf{k}}) \end{pmatrix} U^{\dagger}_{\mathbf{k}}. \tag{11}$$

We can now define a quantity $\chi(Q)$, known as the pair susceptibility, which has been introduced in previous papers; it is a natural extension of $\chi(0)$ and appears in $\Gamma(Q)$:

$$\chi(Q) \equiv \frac{1}{2}\mathrm{Tr}\left[\sum_K G(K)\,\widetilde{G}_0(K - Q)\right], \tag{12}$$

where $\widetilde{G}_0(K) = i\sigma_y [G_0(-K)]^T i\sigma_y$ is the time-reversed, or hole, Green's function.

Substituting the above definitions then gives

$$\begin{aligned} \chi(Q) &= \frac{1}{2}\mathrm{Tr}\left[\sum_K \sum_{\eta\alpha} \frac{P_{\eta\alpha}(\mathbf{k})}{i\nu - \eta E_{\alpha\mathbf{k}}} \sum_{\alpha'} \frac{P^0_{\alpha'}(\mathbf{k} - \mathbf{q})}{i\nu - i\omega + \xi_{\alpha'\mathbf{k}-\mathbf{q}}}\right], \\ &= \frac{1}{2}\sum_{\mathbf{k}} \sum_{\eta\alpha\alpha'} \left(\sum_{i\nu} \frac{1}{i\nu - \eta E_{\alpha\mathbf{k}}} \frac{1}{i\nu - (i\omega - \xi_{\alpha'\mathbf{k}-\mathbf{q}})}\right) \\ &\quad \times \mathrm{Tr}\left[P_{\eta\alpha}(\mathbf{k})\, P^0_{\alpha'}(\mathbf{k} - \mathbf{q})\right]. \end{aligned} \tag{13}$$

Performing the summation over Matsubara frequencies

reduces this expression to

$$\chi(Q) = \frac{1}{2}\sum_{\mathbf{k}}\sum_{\eta\alpha\alpha'}\left(\frac{f(\eta E_{\alpha\mathbf{k}}) - f(-\xi_{\alpha'\mathbf{k}-\mathbf{q}})}{i\omega - (\eta E_{\alpha\mathbf{k}} + \xi_{\alpha'\mathbf{k}-\mathbf{q}})}\right) \times v_{\eta\alpha\alpha'}(\mathbf{k}, \mathbf{k}-\mathbf{q}). \quad (14)$$

Here the coherence factor discussed in Eq. (3) and Eq. (4) of the main text is

$$v_{\eta\alpha\alpha'}(\mathbf{k}, \mathbf{k}-\mathbf{q}) = \mathrm{Tr}\left[P_{\eta\alpha}(\mathbf{k}) P^0_{\alpha'}(\mathbf{k}-\mathbf{q})\right]. \quad (15)$$

The vertex function can now be defined by $\Gamma(Q) \equiv \left[\chi(Q) + g^{-1}\right]^{-1}$. Using the expression for the susceptibility in Eq. (14), we obtain the vertex function $\Gamma(Q)$ as given in Eq. (4) of the main text. The familiar gap equation can then also be obtained from the Thouless criteria: $\chi(0) + g^{-1} = 0$.

We now derive the density-density and spin-spin correlation functions for the normal phase ($T > T_c$) in the presence of SOC and a Zeeman field. In the normal phase there are no collective-mode contributions. The density-density or spin-spin correlation functions, as in the main text, can be written as $\chi_{S_iS_j}(Q) \equiv \int d\tau\, e^{i\omega\tau} \langle T_\tau S_{\mathbf{q}i}(\tau) S_{-\mathbf{q}j}(0)\rangle$, for a many-body density or spin operator $S_{\mathbf{q}i} = \sum_{ss'\mathbf{k}} c^\dagger_{\mathbf{k}s}(\sigma_i)_{ss'} c_{\mathbf{k}+\mathbf{q}s'}$. Here $i = j = 0$, with $\sigma_0 = \mathbb{1}_2$, corresponds to the density-density correlation function $\chi_{\rho\rho}(Q)$, and $i, j \in \{x, y, z\}$ gives the corresponding spin-spin correlation function.

We emphasize that in the normal state there is no anomalous Green's function component, but the existence of normal state pairs allows one to write the correlation functions as the sum of two terms

$$\chi_{S_iS_j}(Q) = \sum_K \mathrm{Tr}\left[\sigma_i G(K)\sigma_j G(K+Q) + \sigma_i F(K)\sigma_j \widetilde{F}(K+Q)\right]. \quad (16)$$

Here we associate $F(K) = (\Delta/\Delta^*)\widetilde{F}(K)$ with a pseudogap vertex contribution, which leads to

$$\chi_{S_iS_j}(Q) = \sum_K \sum_{\alpha\alpha',\eta\eta'} \frac{1}{i\nu - \eta E_{\alpha\mathbf{k}}} \frac{1}{i\nu + i\omega - \eta' E_{\alpha'\mathbf{k}+\mathbf{q}}} \times w_{\alpha\alpha',\eta\eta'}(\mathbf{k}, \mathbf{k}+\mathbf{q}), \quad (17)$$

where we have introduced the coherence factor

$$w_{\alpha\alpha',\eta\eta'}(\mathbf{k}, \mathbf{k}+\mathbf{q}) = \mathrm{Tr}[\sigma_i P_{\eta\alpha}(\mathbf{k})\sigma_j P_{\eta'\alpha'}(\mathbf{k}+\mathbf{q})] + \mathrm{Tr}[\sigma_i Q_{\eta\alpha}(\mathbf{k})\sigma_j R_{\eta'\alpha'}(\mathbf{k}+\mathbf{q})]. \quad (18)$$

Upon performing the summation over Matsubara frequencies, we obtain the expression for the density-density or spin-spin correlation function given in Eq. (6) of the main text.

* brandona@uchicago.edu

[1] N. Read and D. Green, Phys. Rev. B **61**, 10267 (2000).
[2] M. Hasan and C. Kane, Rev. Mod. Phys. **82**, 3045 (2010).
[3] X.-L. Qi and S.-C. Zhang, Rev. Mod. Phys. **83**, 1057 (2011).
[4] J. Alicea, Rep. Prog. Phys. **75**, 076501 (2012).
[5] L. Fu and C. L. Kane, Phys. Rev. Lett. **100**, 096407 (2008).
[6] C. Zhang, S. Tewari, R. Lutchyn, and S. DasSarma, Phys. Rev. Lett. **101**, 160401 (2008).
[7] M. Sato, Y. Takahashi, and S. Fujimoto, Phys. Rev. Lett. **103**, 020401 (2009).
[8] H. Zhai, Rep. Prog. Phys. **78**, 026001 (2015).
[9] M. Iskin and A. L. Subaşı, Phys. Rev. Lett. **107**, 050402 (2011).
[10] W. Yi and G.-C. Guo, Phys. Rev. A **84**, 031608 (2011).
[11] J. Zhou, W. Zhang, and W. Yi, Phys. Rev. A **84**, 063603 (2011).
[12] P. Wang, Z.-Q. Yu, Z. Fu, J. Miao, L. Huang, S. Chai, H. Zhai, and J. Zhang, Phys. Rev. Lett. **109**, 095301 (2012).
[13] L. W. Cheuk, A. T. Sommer, Z. Hadzibabic, T. Yefsah, W. S. Bakr, and M. W. Zwierlein, Phys. Rev. Lett. **109**, 095302 (2012).
[14] L. Huang, Z. Meng, P. Wang, P. Peng, S.-L. Zhang, L. Chen, D. Li, Q. Zhou, and J. Zhang, ArXiv e-prints (2015), arXiv:1506.02861 [cond-mat.quant-gas].
[15] L. Jiang, X.-J. Liu, H. Hu, and H. Pu, Phys. Rev. A **84**, 063618 (2011).
[16] K. Seo, C. Zhang, and S. Tewari, Phys. Rev. A **87**, 063618 (2013).
[17] M. Gong, S. Tewari, and C. Zhang, Phys. Rev. Lett. **107**, 195303 (2011).
[18] Z.-Q. Yu and H. Zhai, Phys. Rev. Lett. **107**, 195305 (2011).
[19] H. Hu, L. Jiang, X.-J. Liu, and H. Pu, Phys. Rev. Lett. **107**, 195304 (2011).
[20] L. Han and C. A. R. deMelo, Phys. Rev. A **85**, 011606(R) (2012).
[21] J. P. Vyasanakere, S. Zhang, and V. B. Shenoy, Phys. Rev. B **84**, 014512 (2011).
[22] K. Seo, C. Zhang, and S. Tewari, Phys. Rev. A **87**, 063618 (2013).
[23] Z. Zheng, H. Pu, X. Zou, and G. Guo, Phys. Rev. A **90**, 063623 (2014).
[24] K. Seo, L. Han, and C. A. R. Sá de Melo, Phys. Rev. A **85**, 033601 (2012).
[25] T. Ojanen and T. Kitagawa, Phys. Rev. B **87**, 014512 (2013).
[26] G. Veeravalli, E. Kuhnle, P. Dyke, and C. J. Vale, Phys. Rev. Lett. **101**, 250403 (2009).
[27] Y.-J. Kao, Q. Si, and K. Levin, Phys. Rev. B **61**, R11898 (2000).
[28] A. J. A. James, R. M. Konik, and T. M. Rice, Phys. Rev. B **86**, 100508 (2012).
[29] Y. J. Lin, K. Jimenez-Garcia, and I. B. Spielman, Nature **471**, 83 (2011).
[30] J. Higbie and D. M. Stamper-Kurn, Phys. Rev. A **69**,

053605 (2004).
[31] W. Ketterle and M. W. Zwierlein, Rivista del Nuovo Cimento **31**, 247 (2008).
[32] Q. J. Chen, J. Stajic, S. N. Tan, and K. Levin, Phys. Rep. **412**, 1 (2005).
[33] C.-T. Wu, B. M. Anderson, R. Boyack, and K. Levin, Phys. Rev. B **91**, 220504(R) (2015).
[34] Q. J. Chen, I. Kosztin, B. Jankó, and K. Levin, Phys. Rev. Lett. **81**, 4708 (1998).
[35] (), however, within the widely used saddle point approximation, the effective vertex obtained via the path integral can only include Green's functions in a symmetric manner.
[36] (), since $\Gamma(0, \mathbf{q})$ will be symmetric in $\mathbf{q}$ for inversion-symmetric systems, the first and third order terms in $\mathbf{q}$ will vanish, and the lowest correction will come in at fourth order.
[37] P. Pieri, L. Pisani, and G. C. Strinati, Phys. Rev. B **70**, 094508 (2004); R. Haussmann, W. Rantner, S. Cerrito, and W. Zwerger, Phys. Rev. A **75**, 023610 (2007); N. Fukushima, Y. Ohashi, E. Taylor, and A. Griffin, *ibid.* **75**, 033609 (2007); H. Hu, P. D. Drummond, and X. J. Liu, Nat. Phys. **3**, 469 (2007).
[38] (), one can improve on this approach, [see J. Maly et al, Physica C 321, 113 (1999) and He et al, PRB 76, 224516 (2007)] but the added complexity does not affect T_c and does not lead to new physics.
[39] J. T. Stewart, J. P. Gaebler, and D. S. Jin, Nature **454**, 744 (2008).
[40] C.-Y. Wang and Y. He, ArXiv e-prints (2015), arXiv:1506.07064 [cond-mat.quant-gas].